ACS OMEGA

http://pubs.acs.org/journal/acsodf

Article

Structural and Magnetic Characterization of Nd−Pr−Fe−B Sintered Magnet Machining Wastes

Karen Bolis,* Gabriela Silva Goulart, Alisson Carlos Krohling, Renato Mendonça, Luis Eugenio Fernandez-Outon,* and José Domingos Ardisson*

Cite This: *ACS Omega* 2023, 8, 12246−12258

Read Online

ACCESS | Metrics & More | Article Recommendations

ABSTRACT: Nd−Pr−Fe−B sintered magnets are considered important for emerging technologies. They are fundamental to the energy matrix transition, such as electric and hybrid vehicles and wind turbines. The production of these magnets generates tons of residues in the machining process step. Since China dominates the rare-earth (RE) market, leading to supply shortages, processing wastes are a promising alternative for recycling or reusing RE materials. Due to the amount generated and the chemical composition, containing up to 30 wt % of critical rare-earth elements, the studies of RE magnets are expanding in the current circular economy scenario. In this work, Nd−Pr−Fe−B machining wastes from two different machining processes (diamond cutting and grinding) were characterized by X-ray diffraction, Mössbauer spectroscopy, vibrating sample magnetometer with first-order-reversal-curves, scanning electron microscopy, X-ray fluorescence, elemental analysis, and X-ray photoelectron spectroscopy. The results showed that the degradation of the phases in both wastes is relatively strong. The phases of the magnets are decomposed into oxides, hydroxides, and hydrated oxides such as $Nd(OH)_3$, ferrihydrite, and metallic iron. In addition, the machining process provokes a change in the iron vicinity of the $Nd_2Fe_{14}B$ phase. The presence of impurities and the wide dispersion of particle sizes resulted in low magnetic properties and affected the magnetization behavior of the machining waste. Using different characterization techniques, it was found that the oxides formed during the machining processes are located on the surfaces of the particles, while the center consists of a nondegraded $Nd_2Fe_{14}B$ phase. It was also found that the Nd−Pr−Fe−B wastes have similarities, indicating that it is possible to mix wastes from different machining processes before recycling. The complete characterization of the Nd−Pr−Fe−B machining residues indicated that different reuse and recycling strategies can be evaluated to improve the efficiency of reusing these machining wastes as secondary sources.

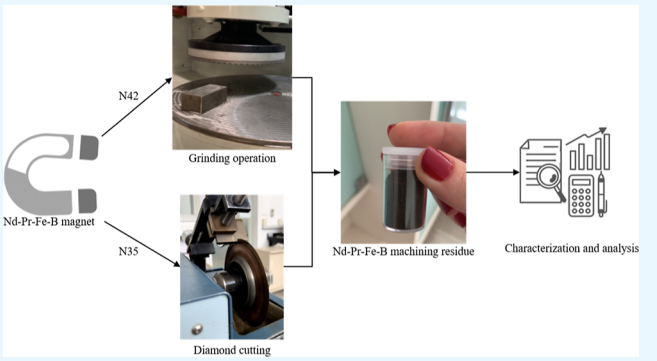

INTRODUCTION

Rare-earth-based magnets economically dominate the permanent magnet market. When compared to the common transition-metal-based magnets, rare-earth magnets present higher magnetic properties such as remanence and coercivity.[1] Among permanent magnets, those based on Nd−Pr−Fe−B are responsible for the largest capital flow in the market. New applications drive the growth of demand for these high-performance magnets.[2] They are used in electrical and electronic devices, motors, electric and hybrid cars, industrial machinery, and wind turbines, making them important for technological applications and the energy transition.[1]

China dominates the rare-earth market, both in terms of supply chain and processing capability of rare-earth elements. In 2020, it was responsible for 92 % of the world's annual magnet production, the highest value-added step in the production chain.[1] To reduce economic dependence, several countries are seeking alternatives to become self-sufficient in terms of these materials and their processing as a strategic activity.[3] Among the possible options, there is a growing interest in recycling and circular economy as this allows the manufacture of products from secondary sources, that is, reduces the exploitation of natural resources.[4−8]

More than 90 % of Nd−Pr−Fe−B magnets are produced by the sintering process. To meet the growing market demand, the production of magnets based on Nd−Pr−Fe−B is being expanded, which leads to an increase in waste during the processing steps. A machining step is mandatory in the production of sintered magnets. Up to 30 wt % of the as-

Received: December 29, 2022
Accepted: February 21, 2023
Published: March 22, 2023

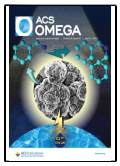

https://doi.org/10.1021/acsomega.2c08249
ACS Omega 2023, 8, 12246−12258

sintered material is wasted in this step.[9,10] The use of processing waste from Nd−Pr−Fe−B magnets is a promising alternative to recycling due to the volume and chemical composition of the waste produce as it contains up to 30 wt % of rare earth, which are considered critical elements due to their ubiquity in high-demand technological applications.[11] Moreover, these production wastes require careful storage. Due to their pyrophoricity, they are considered hazardous as they react vigorously with oxygen.

Nd−Pr−Fe−B sintered magnets consist of a ferromagnetic phase $RE_2Fe_{14}B$ (RE = Nd and Pr) and an RE-rich thin intergranular phase, formed by the segregation of RE atoms at grain boundaries. The magnetic nature of this RE-rich phase determines the degree of exchange coupling between $RE_2Fe_{14}B$ grains, leading to a decrease in coercivity (H_C) when they are ferromagnetic. H_C is expected to increase when non-ferromagnetic intergranular phases are formed, leading to exchange decoupling between ferromagnetic grains.[12]

In sintered Nd−Pr−Fe−B magnet machining processes, oxygen from air is the major contaminant. Kim evaluated the effects of oxygen on the magnetic properties of Nd−Fe−B magnets and found that the magnetic properties gradually decreased with increasing oxygen content.[13] This deterioration is due to the degradation of the RE-rich phase[14] as this phase is most susceptible to oxidation. Powders containing large amounts of oxygen exhibit decreased content of RE-rich phase, resulting in low-density sintered magnets and decreased magnetic properties, such as H_C and $(BH)_{max}$, due to insufficient exchange-decoupling of ferromagnetic grains.[15]

Oxygen also reacts with the $RE_2Fe_{14}B$ phase. Edgley et al.[16] studied the oxidation of bulk samples of Nd−Fe−B in a pure oxygen atmosphere (above 500 °C) and in air (temperatures between 350 and 600 °C). In a pure oxygen atmosphere, three exothermic reactions occurred corresponding to the oxidation of the Nd-rich intergranular regions, to the matrix phase $Nd_2Fe_{14}B$, and the α-Fe formed during the oxidation of the $Nd_2Fe_{14}B$ phase. The matrix phase dissociated and formed an adherent surface layer that grew transgranular instead of occurring along the grain boundaries, probably due to a reaction in the Nd-rich regions that prevented rapid diffusion of oxygen along the grain boundaries The dissociation of the $Nd_2Fe_{14}B$ matrix into α-Fe nanocrystals was observed, which contained small precipitates of oxides, such as Fe_2O_3, NdO, and Nd_2O_3, from oxidation of the RE-rich phase.[16]

When Nd−Pr−Fe−B alloys are in powder form, the oxidation rate is higher than that of solid materials. Therefore, there is a relationship between the particle size and the kinetic parameters of the dissociation of the $Nd_2Fe_{14}B$ phase.[14] The larger oxidation rate may be related to the increase in the surface area of the powder particles and the resulting increased surface reaction with atmospheric oxygen.[17] Despite the higher oxidation rate, the oxidation mode and oxidation products are similar to the bulk samples.[18]

In an aqueous environment, as is the case in machining processes, the reactions are different. Tokuhara et al. investigated the corrosion mechanism of Nd−Fe−B magnets in a high-humidity environment. The authors observed a mixture of $Nd(OH)_3$, $Nd_2Fe_{14}B$, and $Nd_{1.1}Fe_4B_4$ in the dust layer formed in the tested magnet, which was coated with a corrosion protection layer. They attributed the corrosion mechanism of selective oxidation at the grain boundaries of the Nd-rich phase to the $Nd(OH)_3$ form.[19] The selective dissolution of the grain boundaries causes the $Nd_2Fe_{14}B$ grains to detach without significant oxidation.[20]

The selective oxidation process shown in the following equations should be considered when analyzing machining waste.[21,22]

$$(Nd, Pr)Fe_{14}B + H_2O \rightarrow Nd + Pr + 14Fe + B + H_2O \quad (1)$$

$$Nd + 3H_2O \rightarrow Nd^{3+} + 3OH^- + 3H^+ + 3e \rightarrow Nd(OH)_3 + 3H^- + 3e \text{ (in solution)} \quad (2)$$

$$Nd(OH)_3 \rightarrow NdO(OH) + H_2O \quad (3)$$

$$2NdO(OH) \rightarrow Nd_2O_3 + H_2O, \text{ similarly} \quad (4)$$

$$Pr + 3H_2O \rightarrow Pr^{3+} + 3OH^- + 3H^+ + 3e \rightarrow Pr(OH)_3 + 3H^+ + 3e \text{ (in solution)} \quad (5)$$

$$Pr(OH)_3 \rightarrow PrO(OH) + H_2O \quad (6)$$

$$2PrO(OH) \rightarrow Pr_2O_3 + H_2O \quad (7)$$

Currently, RE−Fe−B machining waste is used for indirect recycling to recover rare-earth elements.[5,23,24] This multistep process recovers a high percentage of rare-earth elements. On the other hand, indirect recycling involves high processing costs, a high volume of liquid waste, and an environmentally harmful CO_2 footprint.[25] Another recycling strategy that receives researchers' attention is direct or alloy recycling, where the end product is a material that can be reinserted directly into the production chain.[4] One of the processes being investigated to do that is the calciothermic reduction process, where the magnetic alloy is directly recovered.[26−31] The decision process for a recycling route takes into account economic and technical aspects such as process costs, efficiency, and environmental impact.

The existing literature on the recycling of RE−Fe−B machining wastes focuses on the processes used, while the properties of the feedstock are hardly addressed.[9,10,26−29,32−34] Particle morphology, chemical composition, and phases present in machining wastes are often addressed and, in some cases, particle size analysis is also shown.[9,10,28−32,34]

More recently, Xu et al. showed the improvement of magnetization of recycled Nd−Fe−B machining sludge due to the effectiveness of the recycling process used.[28,29] They showed that the Nd−Fe−B sintered magnet machining waste was mainly composed of the $Nd_2Fe_{14}B$ phase and had a high oxygen and carbon content, which affected the magnetic properties and made the direct reuse into the production of Nd−Pr−Fe−B magnets unfeasible. However, not enough structural and magnetic information about the sludge was found to understand the effects of the machining processes on the magnetic properties of the Nd−Pr−Fe−B waste and to help optimize the recycling processes.

As mentioned earlier, sintered Nd−Pr−Fe−B machining wastes are promising materials for recycling due to their high content of critical rare-earth elements. Since various processes can be used to machine sintered magnets, it is important to understand their effects on the characteristics of the resulting machining sludges, especially before using these materials in recycling routes. Therefore, it is expected that a detailed knowledge of the characteristics of machining residues and the

https://doi.org/10.1021/acsomega.2c08249
ACS Omega 2023, 8, 12246−12258

evaluation of the feasibility of different machining processes on the magnetic, structural, and morphological characteristics of waste residues should support the optimization of the recycling processes used.

The objective of this study is to evaluate the structural and magnetic characteristics of Nd−Pr−Fe−B machining residues produced by two different common machining processes for sintered magnets. One process involves cutting the magnet with a diamond cutting wheel, and other involves a grinding operation.

EXPERIMENTAL SECTION

Samples. Nd−Pr−Fe−B magnets are hard (Vickers hardness 600), brittle (tensile strength 100 MPa), and a very appropriate material to use the same technologies used to machine ceramics for their production.[35] Due to their mechanical properties, Nd−Pr−Fe−B sintered magnets are considered difficult to machine by conventional machining processes. Some processes used industrially to machine Nd−Pr−Fe−B magnets are electrical discharge machining, grinding operations, and the use of diamond tools. While some papers do not specify which machining process was used, others mention that the sludges studied were obtained in grinding operations using an epoxy-resin-bonded diamond grinding wheel[34] and a multiwire cutting process.[29]

The sintered Nd−Pr−Fe−B magnet machining sludges investigated here originated from two different machining processes, both of which are used in the production chain of sintered magnets. The first machining residue investigated originated from a cutting process using a diamond wheel, and the second was from a grinding operation using an alumina wheel.

Samples of diamond cut machining residue were obtained in the laboratory on a cutting bench. A commercial Nd−Pr−Fe−B-based magnet, class N42, was cut using a 15-series diamond cutting wheel (LC Diamond, Buehler). The cutting fluid used was a water solution containing 10% in volume of ECOCOOL SYN 1977 BF, soluble type (Fuchs Lubricants of Brazil). From this point, the machining residues generated by this process are called diamond cut residues.

After the machining processes, the wastes were collected and cleaned. The same cleaning procedure as described by Yue[31] was applied to the diamond cut residue. In this process, first water is added to the material after it is immersed in an ultrasonic bath for 5 min so that the particles are released and then dried in an oven at around 85 °C.

The grinding residues were obtained by machining Nd−Pr−Fe−B magnet class N38 on an industrial machine with a vertical axis and rotary table surface grinding machine. The fluid used was a 5 % solution of Syntilo 9902 (Castrol SDS). This is a synthetic oil-based fluid, with additives to protect machine tools and parts from corrosion; it does not contain mineral oil or formaldehyde-releasing agents. The machining residues produced by this process will be called grinding residues in the text.

To remove the machining oil-based fluid from the grinding residues, a method by Xu et al.[28] was used, in which the purification was carried out by alcohol centrifugation and vacuum drying at room temperature. The process for cleaning the grinding residues was carried out using alcohol as the cleaning fluid, a 5 min ultrasonic cleaning bath, and drying at around 85 °C.

Characterization. Various characterization techniques have been used to study how the degradation of crystallographic phases and magnetic properties occurs in the machining waste samples. Scanning electron microscopy (SEM) with backscattered electrons was used to analyze particle morphology and surface changes due to machining effects. Particle size analysis by laser diffraction was used to determine particle size distribution. X-ray fluorescence (XRF) and elemental analysis were used to determine chemical composition. X-ray diffraction (XRD) was used to determine crystallographic phases. X-ray photoelectron spectroscopy (XPS) was used to evaluate the valence states and initial degradation of the samples. Mössbauer spectroscopy (MS) was used to quantify how the machining process affects the environment of the iron atoms in $Nd_2Fe_{14}B$. Vibrating sample magnetometer (VSM) with first-order-reversal-curves (FORCs) was used to evaluate magnetic properties and particle interaction.

Particle size distribution was determined using laser diffraction particle size analysis (Mastersizer 3000). The analysis was performed using the Fraunhofer scattering model[36] and a dry dispersion method.[37]

XRF measurement was performed using an XRF spectrometer. Oxygen content was measured by the inert gas melting method[38] (ONH836, LECO), and the carbon content was determined by direct combustion and infrared detection (CS 300, LECO).

XRD measurements were performed in Bragg−Brentano geometry with Cu Kα radiation (λ = 1.540560 Å) and a 2θ measurement range from 10 to 90°. The high-resolution data were refined using the Rietveld method and FullProf Suite software.[39] The crystallographic information files used to refine the measured diffraction patterns were obtained from the Inorganic Crystal Structure Database (ICSD) [collection code number: 41393 for the $Nd_2Fe_{14}B$ phase and 399 for the $Nd(OH)_3$ phase].

X-ray photoelectron spectra from the surfaces of the Nd−Fe−B machining sludge samples were measured using a SPECS system equipped with a Phoibos-150 analyzer and an Al Kα (1486.6 eV) monochromatic X-ray source. The base pressure in the ultrahigh-vacuum chamber was maintained around 10^{-10} mbar during acquisition. The high-resolution spectra were acquired with a pass energy of 20 eV and an energy step of 0.1 eV. The C 1s peaks for adventitious carbon at 284.6 eV were used as energy references for the charge shift.

MS measurements were performed at room temperature, without the application of an external magnetic field, with a conventional constant acceleration spectrometer in transmission geometry, using a ^{57}Co source in an Rh matrix. The spectra were adjusted using the NORMOS software package developed by R. A. Brand.[40] Isomeric deviations were standardized relative to natural Fe (α-Fe).

The magnetic properties of the powders were measured at room temperature with a maximum applied field of 1.5 T and a sweep rate of 0.003 T/s using a LakeShore, model 7404 VSM.

FORCs provide information not apparent from major hysteresis loops. FORC curves provide information on the distribution of switching and interaction fields and identify multiple phases in composite or hybrid materials containing more than one phase. A FORC is measured by saturating a sample in a field H_S, decreasing the field to a reversal field H_A, and then measuring moment versus field H_B as the field is swept back to H_S. This process is repeated for many values of

https://doi.org/10.1021/acsomega.2c08249
ACS Omega 2023, 8, 12246−12258

H_A, yielding a series of FORCs. The measured magnetization at each step as a function of H_A and H_B gives $M(H_A, H_B)$, which is then plotted as a function of H_A and H_b in field space. The FORC distribution $\rho(H_A, H_B)$ is the mixed second derivative.[41]

$$\rho(H_A, H_B) = -\frac{1}{2}\frac{\partial^2 M(H_A, H_B)}{\partial H_A \partial H_B} \quad (8)$$

When plotting a FORC distribution, it is convenient to change the coordinates from $\{H_A, H_B\}$ to $H_C=(H_B-H_A)/2$, $H_U=(H_A + H_B)/2$. A FORC diagram is a 2D contour plot of a FORC distribution with H_C and H_U on the horizontal and vertical axes, respectively. H_U represents the distribution of interaction or reversal fields and H_C represents the distribution of switching or coercive fields of hysterons (fundamental hysteretic entities that may be directly associated with ferromagnetic particles and/or even ferromagnetic domains).[41]

A FORC diagram not only provides information about the distribution of interaction and switching fields but also serves as a "fingerprint" that provides information about the domain state and the nature of interactions occurring in magnetic materials. In a FORC diagram, fully closed contours are usually associated with single-domain (SD) behavior, while open contours that diverge in the direction of the H_U axis are associated with the multidomain (MD) state, while open and closed contours together are associated with pseudo-SD (PSD) behavior. The term "PSD" empirically describes a continuous transition between SD and MD behavior. The PSD range can also be populated by strongly interacting SD particles, as well as binary or ternary mixtures of SP, SD, and MD particles.[42]

RESULTS AND DISCUSSION

Morphology and Particle Size. The particles of the machining sludges (Figure 1) are irregularly shaped due to the brittle mechanical behavior of the $Nd_2Fe_{14}B$ phase. SEM images indicate that grinding residue samples have larger particle sizes than the samples of diamond cut residue.

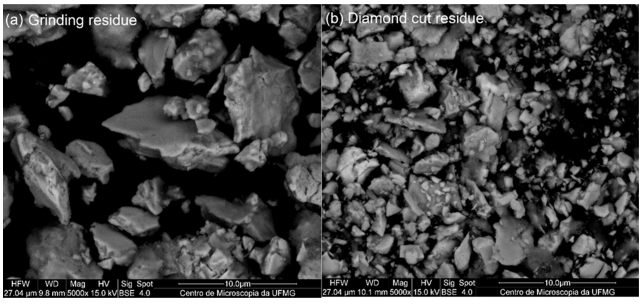

Figure 1. SEM morphology of the (a) grinding residue and (b) diamond cut residue.

Measurements of the particle size distribution (Figure 2) showed that both machining wastes had a nonmodal distribution. Grinding residues exhibited a mean particle size of $\bar{D}_{GR}$ = 6.12 μm, while the mean particle size of the diamond cut residues is smaller $\bar{D}_{DCR}$ = 4.28 μm. The values found are consistent with the mean grain size of Nd−Fe−B-based magnets found in the literature. In the case of machining waste samples, $\bar{D}$ has been found to vary between 3.0 and 3.2 μm,[9,10,28−30] although 1.1 μm[32] was also reported. It is important to consider that larger values of particle sizes for both types of residues may be related to agglomeration due to magnetic interactions between particles of the machining residue.

A lognormal function of the form shown in eq 9 was used to determine the particle size distribution (Figure 2a,b).[43]

$$f(D)dD = \frac{1}{\sqrt{2\pi}\sigma D}\exp\left(-\frac{(\ln(D)/\bar{D})^2}{2\sigma^2}\right) \quad (9)$$

The particle size distributions measured for each sample had several local maxima due to the wide range of particle sizes measured. Therefore, it was necessary to use a superposition of multiple distributions to fit each measurement. The area under the curve for each lognormal distribution is given by A, introduced as a multiplying factor in eq 9. The fitted parameters were the area under the curve (A), the standard deviation (σ) of $\ln(D)$, and the mean diameter ($\bar{D}$). The fitting of the multimodal particle size distributions required the use of 5 and 4 distributions for grinding and diamond cut residues, respectively.

Analysis of the fitting parameters (Table 1) revealed that both residues had similarities in particle size distribution. Both residues presented a similar trend, that is, the most populated distributions; those with the largest area under the curve had $\bar{D}$ > 1000 μm, followed by distributions with $\bar{D} \approx 8$ μm. The wide range of D values in these samples will contribute to reduce their BxH energy product.

Chemical Composition. The chemical compositions obtained from the XRF measurements are shown in Table 2. The rare-earth content in the diamond cut residue (40.96 %) was higher than that in the grinding residue (30.71 %). The Dy content is also higher in the diamond cut residue, but Ce was not found in its composition. This high amount of rare-earth elements found in both cases is consistent with the amount needed to produce magnets.[27] The differences observed between grinding and diamond cut residues should not have an influence on the selected recycling/recovery processes. The chemical composition can vary between magnet producers due to the variety of specifications and application of the related magnetic components.

Elemental analysis indicated that diamond cut sludge samples present oxygen and carbon contents of 6.3 and 1.3 %, which are higher than those found in grinding residue samples, being 4.7 and 0.4 %, respectively. Such differing values may be related to the machining fluid removal. The machining fluid of the diamond cut residue was removed using water, and in the case of the grinding residue, it was used ethanol. An increase of oxygen content from 3 to 7 wt % when the machining sludge was stored underwater was reported by Kruse et al.[34] Both oxygen and carbon content values are similar to published data, e.g.[9,28,29,31,32,34] which show the oxygen content ranging from 5.1 to 16 wt % and the carbon contamination from 0.6 to 2.3 wt %.

Both residues have high rare-earth content, and the major contaminants are oxygen and carbon. Since carbon and oxygen are deleterious to magnetic properties, directly reusing these sludges into sintered magnet production chains is not possible.

Crystallographic Phases. XRD measurements (Figure 3 and Table 3) showed that both residues exhibit two crystalline phases, $Nd_2Fe_{14}B$ and $Nd(OH)_3$. The $Nd_2Fe_{14}B$ crystal structure has a tetragonal structure with space group $P4_2/mnm$, matched with ICSD collection code 41393. According to McCain[20], the $Nd(OH)_3$ phase results from the oxidation of

https://doi.org/10.1021/acsomega.2c08249
ACS Omega 2023, 8, 12246−12258

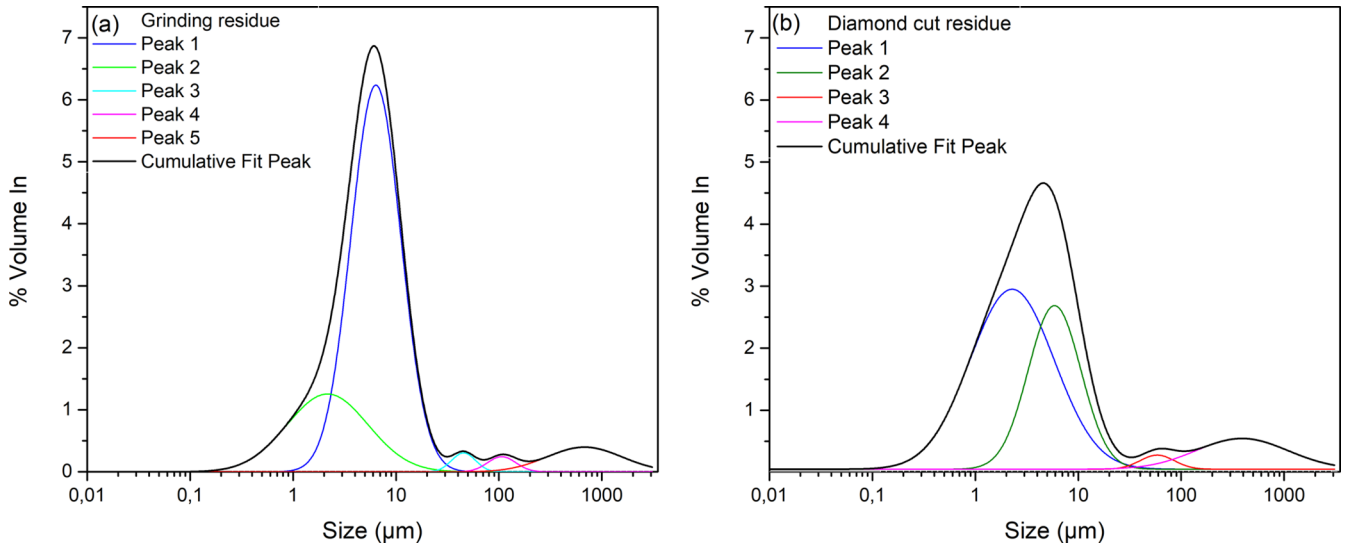

Figure 2. Lognormal function fitting of particle size distributions for the (a) grinding residue and (b) for diamond cut residue.

Table 1. Lognormal Fitting Parameters for Each Distribution Required to Fit the (a) Grinding Residue and (b) for Diamond Cut Residue Particle Size Distribution

	$\bar{D}$ (μm)		σ		A		
	value	std error	value	std error	value	std error	R^2
			(a) Grinding residue				
peak 1	4.91	1.33	0.90	0.07	9.30	2.74	0.99964
peak 2	8.73	0.03	0.56	0.01	65.42	2.38	
peak 3	48.69	0.03	0.27	0.90	9.63	5.25	
peak 4	117.59	5.25	0.32	0.06	21.74	2.11	
peak 5	1364.23	95.25	0.84	0.04	805.68	32.69	
			(b) Diamond cut residue				
peak 1	5.52	1.67	0.94	0.06	24.38	8.90	0.97998
peak 2	28.33	0.35	0.59	0.05	27.25	7.17	
peak 3	67.86	8.42	0.38	0.10	13.76	3.41	
peak 4	1116.49	172.47	1.03	0.09	840.46	60.16	

Table 2. Chemical Composition of Grinding and Diamond Cut Machining Wastes Obtained by XRF Analysis

Element (wt %)	(a) Grinding residue	(b) Diamond cut residue
Nd	21.5 ± 1.08	30.2 ± 1.51
Pr	7.03 ± 0.35	9.62 ± 0.48
Dy	1.29 ± 0.06	2.14 ± 0.11
Ce	0.89 ± 0.04	–
Fe	66.4 ± 3.32	52.4 ± 2.62
Co	1.02 ± 0.05	2.16 ± 0.11
Cu	0.26 ± 0.01	1.07 ± 0.05
Ni	0.03 ± 0.01	0.04 ± 0.01
Al	0.14 ± 0.01	0.18 ± 0.01
P	0.44 ± 0.02	0.54 ± 0.03
Ca	0.21 ± 0.01	0.32 ± 0.02
Nb	0.21 ± 0.01	0.11 ± 0.01
others*[a]	bal.	bal.

[a]Others*: Si, S, Cl, Cr, Zn, Zr, Sn, Ba, and Ga.

the Nd-rich phase in an aqueous environment. Using the Rietveld refinement method, it was possible to identify that both samples are mainly formed by the $Nd_2Fe_{14}B$ phase. This is consistent with the results reported in the literature,[10,28,32,34] which indicate that the sludge samples studied are mainly formed by the $Nd_2Fe_{14}B$ phase. Other phases such as Nd_2O_3, Fe_2O_3, and α-Fe have been found in other studies;[9,29,31] however, they have not been detected in the samples studied in this work. In both samples, the refinement statistics indicated a good fit among experimental and calculated data. For the grinding residue χ^2, Rp and Rwp values are 2.01; 5.62; and 7.17. For the diamond cut residue χ^2, Rp and Rwp values are 5.72; 0.77; and 1.13.

The unit cell parameter values obtained (Table 3) are similar in both samples; they differ from the values expected for the ICSD $Nd_2Fe_{14}B$ phase by less than 0.5 and 0.3 % for the grinding residue and diamond cut residue, respectively, indicating that the $Nd_2Fe_{14}B$ crystalline phase was not significantly affected by the cutting process.

XRD data showed that the Nd-rich phase was oxidized into $Nd(OH)_3$ due to direct contact with water from the cutting fluid. The amount of this phase was higher for the grinding residue sample, indicating that the grinding process resulted in a more accentuated degradation. Also, this technique did not indicate $Nd_2Fe_{14}B$ phase modification.

Mössbauer Spectroscopy. As far as the authors know, there has not been found any published report of ^{57}Fe Mossbauer spectroscopy measurements for Nd−Pr-Fe−B machining sludges, previous to this work. Mössbauer measurements shown in Figure 4 for (a) grinding residue and (b) diamond cut sludge samples were fitted with 11 subspectra. A

https://doi.org/10.1021/acsomega.2c08249
ACS Omega 2023, 8, 12246−12258

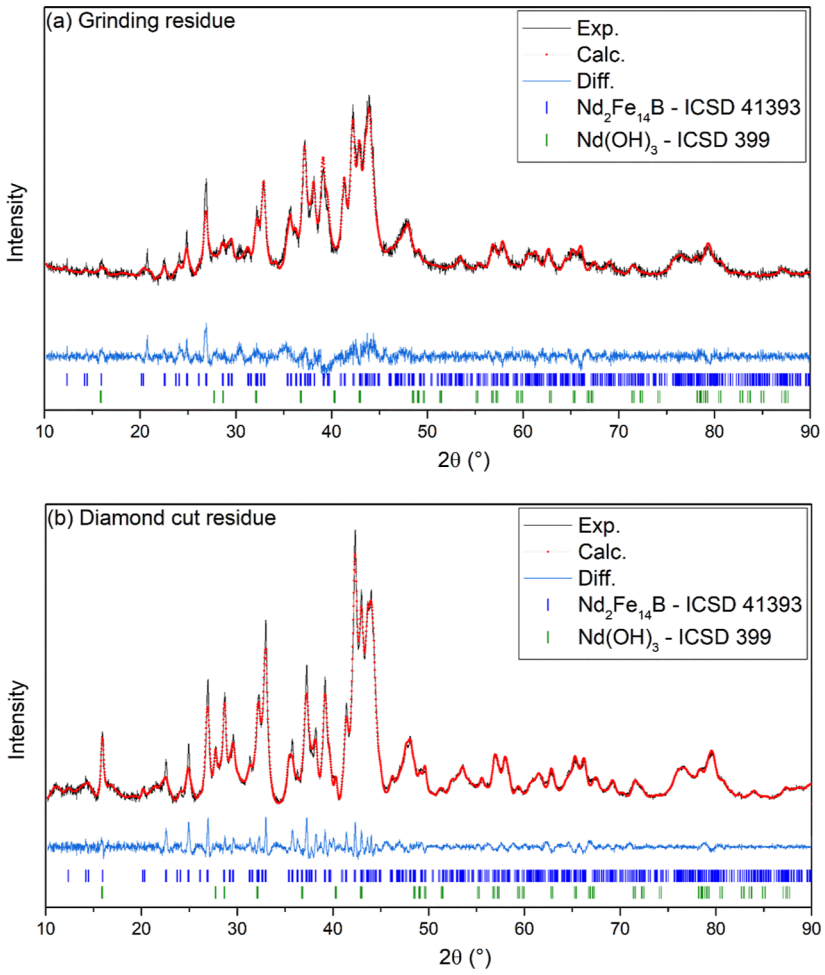

Figure 3. XRD patterns of the (a) grinding residue and (b) diamond cut residue. Black curves are experimental data and red curves are simulated patterns obtained using the Rietveld refinement method. The blue [green] rods refer to the reflection positions that correspond to $Nd_2Fe_{14}B$ [$Nd(OH)_3$ phase].

Table 3. Rietveld Refinement Results for the $Nd_2Fe_{14}B$ Phase in Each Type of Machining Residue.

	χ^2	$Nd_2Fe_{14}B$ phase (%)	a (Å)	c (Å)
ICDS 41393		100	8.800 ± 0.005	12.200 ± 0.007
(a) Grinding residue	2.4	94	8.842 ± 0.002	12.267 ± 0.003
(b) Diamond cut residue	5.6	96	8.829 ± 0.002	12.250 ± 0.003

set of six sextet subspectra are associated with each of the six nonequivalent iron sites in $Nd_2Fe_{14}B$.[44] Table 4 shows the fitting parameters corresponding to each subspectra [relative area (A), isomeric shift (δ), quadrupole shift ($2\varepsilon/\Delta Q$), and hyperfine field (B_{HF})]. The remaining subspectra are a wide sextet with a $B_{HF} \sim 25$ T, which was assigned to a $Nd_2Fe_{14}B$ phase containing defects caused by machining, a sextet attributed to metallic Fe (α-Fe), resulting from the dissociation of the $Nd_2Fe_{14}B$ phase, and three doublets corresponding to nonmagnetic phases, one related to a hydrated iron oxide phase, identified as ferrihydrite [$(Fe^{3+})_2O_3{*}H_2O$], and two iron-based phases with oxidation state Fe^{3+} and Fe^{2+}.

The parameter values shown in Table 4 allow us to analyze the degradation effect of the Fe-containing phases in the sludge samples studied. Note that the relative spectral area of each phase is proportional to its content in the sample. Hence, the sum of the spectral areas corresponding to the six nonequivalent Fe sites of the $Nd_2Fe_{14}B$ phase shows that both types of sludge samples contain similar amounts of such $Nd_2Fe_{14}B$ phase (~69 %). The α-Fe phase is found in similar quantities (~10 %) in both cases.

The hyperfine fields of the $R_2Fe_{14}B$ (R = rare-earth element) compound decrease in the following order: $8j_2 > 16k_2 > 16k_1 > 4e > 8j_1 > 4c$.[44] Any modification in the environment of the Fe atoms at each site may result in the variation of the site-specific B_{HF} value of the $Nd_2Fe_{14}B$ phase, which should be addressed ultimately to a variation in the number of nearest neighbors and species, or in the intensity of the 3d−3d exchange interactions between Fe−Fe atoms or 4f−3d interactions between Nd−Fe atoms, being the latter an order of magnitude weaker. A detailed study for $Nd_2Fe_{14}B$ can be found in Kamal and Andersson[45] and references therein. Kamal and Andersson[45] estimated a 34.4 T average value of B_{HF} for $Nd_2Fe_{14}B$ based on polarized neutron studies by Givord et al.[46] The spectra analyzed have been fitted with a sextet, having reduced B_{HF} 25 T, which has been introduced to account for modifications in the $Nd_2Fe_{14}B$ phase promoted by the machining processes of the magnets. Such processing methods may lead to the migration of Nd to grain boundaries to form Nd-rich phases, resulting in decreased 4f−3d interactions, or

https://doi.org/10.1021/acsomega.2c08249
ACS Omega 2023, 8, 12246−12258

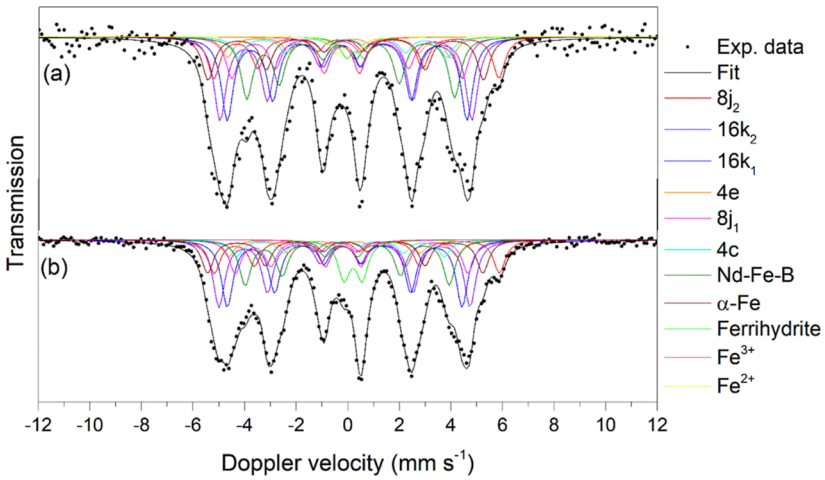

Figure 4. Mössbauer spectra of ^{57}Fe at room temperature of machining residues. (a) Grinding residue and (b) diamond cut residue samples. Experimental data (black dots) and fitted spectrum (black curve). The phases corresponding to each subspectra are shown in the inset.

may involve the formation of α-Fe and other Fe phases, and therefore a reduction in 3d−3d exchange interactions between Fe−Fe neighbors. The relative spectral area corresponding to degraded $Nd_2Fe_{14}B$ is about ∼13 % of the total spectral area in both samples. Hence, approximately 82 % of the Fe spectral area corresponds to $Nd_2Fe_{14}B$ phases. Fe phases corresponding to ferrihydrite [$(Fe^{3+})_2O_3$*H_2O], Fe^{3+}, and Fe^{2+} have been found. The most prominent difference regarding Fe phases is the appearance of Fe^{2+} phases in grinding residue samples. Diamond cut sludge samples exhibit higher amounts of ferrihydrite and Fe^{3+} possibly due to the more effective heat dissipation mechanisms during the machining of the magnets (no Fe^{2+} phases were found).

X-ray Photoelectron Spectroscopy. XPS results (Figure 5) revealed typical signals of Nd 3d, Pr 3d, and Fe 2p in both samples. The Nd 3d peak is fitted with six lines and the Nd $3d_{5/2}$ peak is decomposed in O (KLL) Auger, Nd $3d_{5/2}$ satellite, and Nd $3d_{5/2}$ main peak. The Nd $3d_{5/2}$ at 982.7 eV and the satellite peak at 978.2 eV indicate the trivalent neodymium on the residue surface of both diamond cut residue and grinding residue, with the O (KLL) peak being more intense for the surface of the grinding residue sample.[47]

The Pr 3d peaks point out trivalent praseodymium on the surface of both samples. For the diamond cut residue, Pr 3d peaks are fitted with four lines, the satellite peak at 929.6 eV and the spin−orbit splitting between the Pr 3d peaks equivalent to 20.7 eV.[48,49] For the grinding residue sample, the Pr 3d peaks are fitted with six components. In particular, Pr $3d_{5/2}$ presented three components, two Pr $3d_{5/2}$ main peaks for Pr^{3+} and Pr^{4+} centered at 933.4 and 935.9 eV and another at 928.0 eV corresponding to a satellite related to Pr^{3+}.[50]

The analysis also pointed to the presence of trivalent iron in both samples. The occurrence of the main peak at 710.8 eV and the satellite peak at 720.2 eV is the most important signature that points to trivalent iron on the diamond cut residue surface.[51,52] Differently, for the grinding residue, Fe 2p is decomposed with six components. Fe^0 is denoted by the peak at 707.4 eV and Fe^{3+} is indicated by the peak at 711.2 eV.[53]

XPS analysis showed a large degradation on the surfaces of the machining residues. Also, based on the valence state, it is possible to infer that the degradation process is relatively different for each sample, which may be due to the particularities of the distinct machining processes used to obtain the samples, such as machining tools and heat dissipation mechanisms. The segregation of rare-earth elements from the alloy (as demonstrated in eqs 1−7) caused by the machining process could produce changes in structural and magnetic properties, in particular, for very small particles having increased specific surface area. Knowledge of the compounds formed and the level of degradation that arises during the machining process of Nd−Fe−B magnets could guide the reuse of residue wastes.

Magnetic Properties. To evaluate the magnetic properties of the samples, VSM and FORC measurements were performed (Figure 6). Major hysteresis loops measured with a maximum applied field of 1.5 T, allowed us to obtain coercivity (H_C), magnetization at a maximum applied field of 1.5 T (M), and magnetic remanence (M_R) values for the grinding residue samples and diamond cut samples. The latter exhibited lower values (Table 5). Both remanence and coercivity values are low due to the presence of contaminants and other phases having different magnetic behavior than the $Nd_2Fe_{14}B$ phase. Recent literature reports show machining sludges having M_S in the range of 110−123 Am^2/kg for an applied field of 3 T and low values of coercivity. When the sludge particles are purified to remove the machining fluid, these values are found to increase up to 125−137 Am^2/kg.[28,29]

Structural differences arising from the machining processes due to the deformation of the particles or surface modifications of the Nd−Fe−B grains can affect the magnetic properties of residues. The structural aspects found in the XRD, XPS, and MS results of the machining residues evaluated here can act as nucleation sites for reverse domains and, therefore, decrease the coercivity values.

Figure 6a,b shows the 100 FORC curves obtained for both grinding residue and diamond cut residue samples measured under the same conditions. Using the FORCinel software,[54] FORC data (Figure 6a,b) are converted into the FORC diagrams that allow obtaining the distribution of interaction fields (H_U) and switching fields (H_C) (Figure 6c,d). The samples were measured in powder form; note that the demagnetizing field has not been removed to obtain the effective magnetic field acting on the sample.

The FORC-2D distribution values helped to identify the presence of harder or softer magnetic phases, depending on

https://doi.org/10.1021/acsomega.2c08249
ACS Omega 2023, 8, 12246−12258

Table 4. Hyperfine Parameters at Room Temperature of the Machining Residues: (a) Grinding Residue and (b) Diamond Cut Residue

Long et al.[44] (a) grinding residue and (b) diamond cut residue						
	Occupation					
Site	Fe	Nd	$\delta \pm 0.05$ (mm/s)	$2\varepsilon/\Delta Q \pm 0.05$ (mm/s)	$B_{HF} \pm 0.5$ (T)	Area ± 0.5 (%)
$8j_2$	12	2				
ref. 44			0.08	0.66	34.3	
(a)			0.09	0.62	34.3	9.9
(b)			0.06	0.77	34.3	9.7
$16k_2$	10	1				
ref. 44			−0.12	0.30	30.6	
(a)			−0.11	0.23	30.3	19.7
(b)			−0.11	0.16	30.2	19.5
$16k_1$	9	0				
ref. 44			−0.04	0.30	28.7	
(a)			−0.05	0.20	28.8	19.7
(b)			−0.06	0.17	28.2	19.5
$8j_1$	9	2				
ref. 44			−0.06			
(a)			−0.06	0.27	27.4	9.9
(b)			−0.07	0.28	27.9	9.7
4e	9	3				
ref. 44			−0.01	−0.62	27.8	
(a)			−0.07	−0.65	27.2	4.9
(b)			−0.03	−0.62	27.8	4.9
4c	8	2				
ref. 44			−0.09	−0.30	25.0	
(a)			−0.07	−0.09	25.0	4.9
(b)			−0.13	−0.13	25.0	4.9
Nd−Fe−B						
(a)			−0.03	0.44	25.0	13.4
(b)			−0.03	0.22	24.5	13.1
α-Fe						
(a)			0	0	33.1	9.6
(b)			0	0	33.1	10.1
Ferrihydrite						
(a)			0.37	0.70	–	2.4
(b)			0.30	0.70	–	5.6
Fe^{3+}						
(a)			−0.16	1.37	–	3.9
(b)			−0.08	1.38	–	3.9
Fe^{2+}						
(a)			0.03	0.75	–	1.6
(b)			–	–	–	–

their magnitude, and the number of distributions of these peaks. In both samples, it was observed that there is only one distribution peak, represented by the highest $\rho(H_A, H_B)$ values (more reddish coloration).

Both distributions of interaction and switching fields are influenced by the grain size distribution of the particles within each sample. SEM measurements and laser diffraction particle size analysis revealed the extremely wide distribution of particle size for each type of residue sample, ranging from 10^{-1}−10^{3} μm, having the most populated distribution mode between 1 and 10 μm. In an ensemble of particles where several distribution modes can be found, a variety of coexisting magnetic behaviors were observed. For instance, in the case of sintered magnets with typical grain size in the 10^{-6} m range, the existence of particles smaller than 1 μm influences significantly the magnetization reversal process. Furthermore, the existence of nanosized defects near grain boundaries is also of critical importance in the magnetization reversal process.[55] Note that in the samples studied, the wide range of particle size measured includes particles that must be polycrystalline, formed by several grains, and small particles that may be formed by a single grain.

The possible appearance of soft and hard phases would manifest as magnetization kinks or abrupt variations in the shape of the hysteresis loop on the magnetization axis, proportional to the relative abundance of each magnetic phase. Note that the coercivity of ferromagnetic particles varies nonmonotonically with the particle size, and above the critical size for single-domain behavior, it increases with decreasing size. This critical size for Nd−Fe−B is 0.1 μm for the $Nd_2Fe_{14}B$ phase.[56] Ramesh and Srikrishna[57] showed that H_C varies inversely to the logarithm of the surface of the grains. Therefore, for a multimodal distribution of noninteracting particle sizes, a kink in magnetization would be observed for

https://doi.org/10.1021/acsomega.2c08249
ACS Omega 2023, 8, 12246−12258

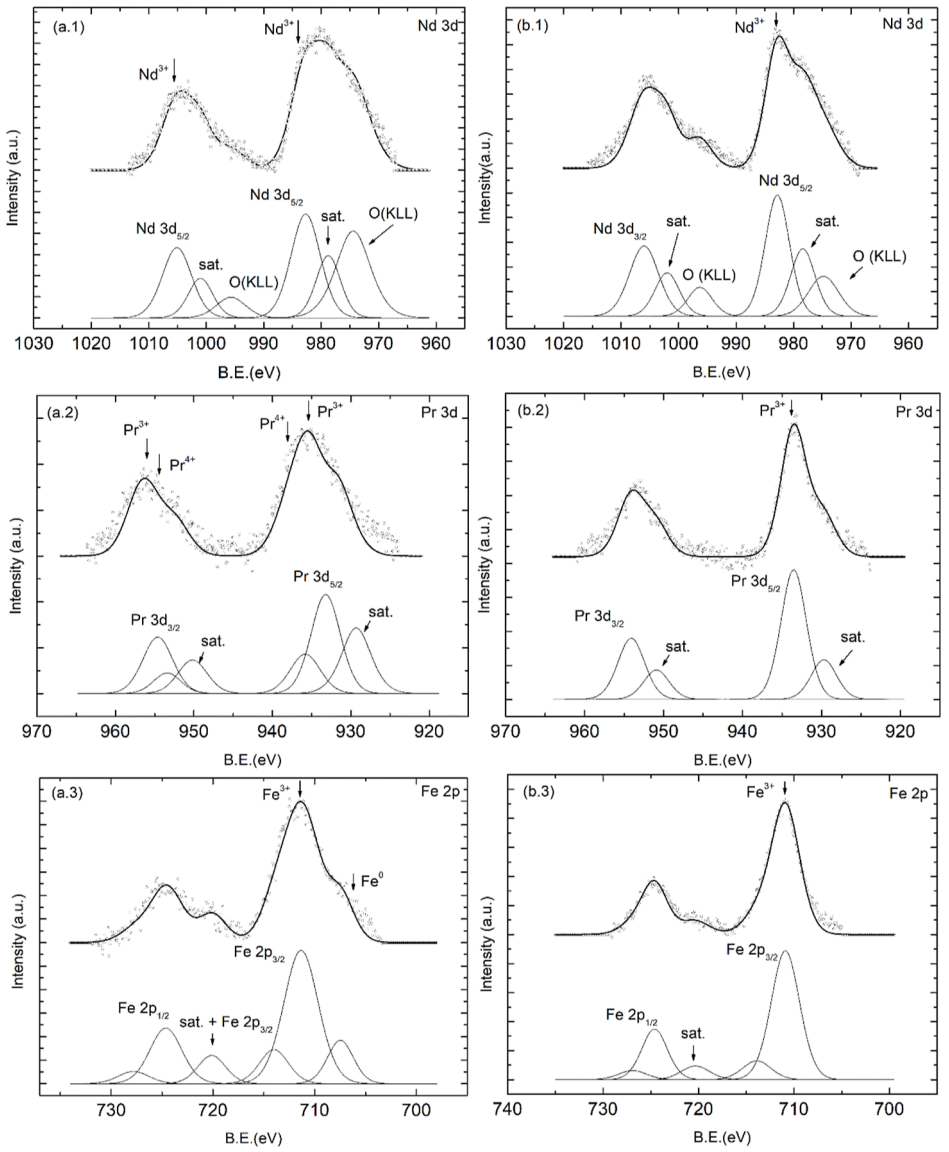

Figure 5. XPS detailed spectra of machining residues: (a) 1−3 grinding residue and (b) 1−3 diamond cut residue.

each mode in the particle size distribution, each having a characteristic switching field distribution. On the other hand, magnetostatic interactions between particles may lead to particle agglomeration and the concomitant formation of closed loops of magnetization chains that would affect both coercivity and magnetization values.

It should be noted in Figure 6a,b that no evident kink in magnetization has been observed, which may be attributed to particle agglomeration, or even a particle rotation within the powder samples studied. Also, a large number of particles with low coercivity, as expected for $Nd_2Fe_{14}B$ particles with a mean diameter less than 3.0 μm,[56] should induce a magnetization reversal of particles with larger H_C if particle interactions are significant. Figure 6c,d exhibits continuous and wide distributions on the values of H_U (y-axis) and H_C (x-axis). It is noteworthy that grinding residue samples exhibit stronger magnetostatic interactions H_U for particles with H_C less than 0.2 T compared to diamond cut residues. Its switching field distribution is also larger. The H_C peak for this sample is centered at a much lower value than that of diamond cut residue samples, which may be related to the larger average particle size. The latter exhibits narrower H_U and H_C distributions. The FORC diagram obtained for diamond cut residues shows a wide distribution of coercivities with the peak of the distribution centered at $H_C \sim 0.04-0.14$ T (first contour) and magnetic interactions centered at $H_U \sim 0.006$ T. It is possible to observe that particles $H_C < 0.1$ T also exhibit a wider spread along the H_U axis than that for hard-phase particles, indicating that the smallest particles experience stronger magnetostatic coupling than those with larger H_C. However, grinding residue samples show a larger portion of low-coercivity particles, observed as a peak of lower intensity centered at $H_C < 0.08$ T, which experience a wider and more asymmetric distribution of magnetostatic interactions than that observed for the diamond cut particles with similar coercivity.

The large distributions of particle sizes observed in both samples hamper the interpretation of the FORC diagrams measured. Following the description provided in Ramesh and Srikrishna,[57] it may be argued that diamond cut samples exhibit a FORC diagram that may be assigned to single-domain particles based on the closed contours observed; however, grinding residues also exhibit contours that diverge

https://doi.org/10.1021/acsomega.2c08249
ACS Omega 2023, 8, 12246−12258

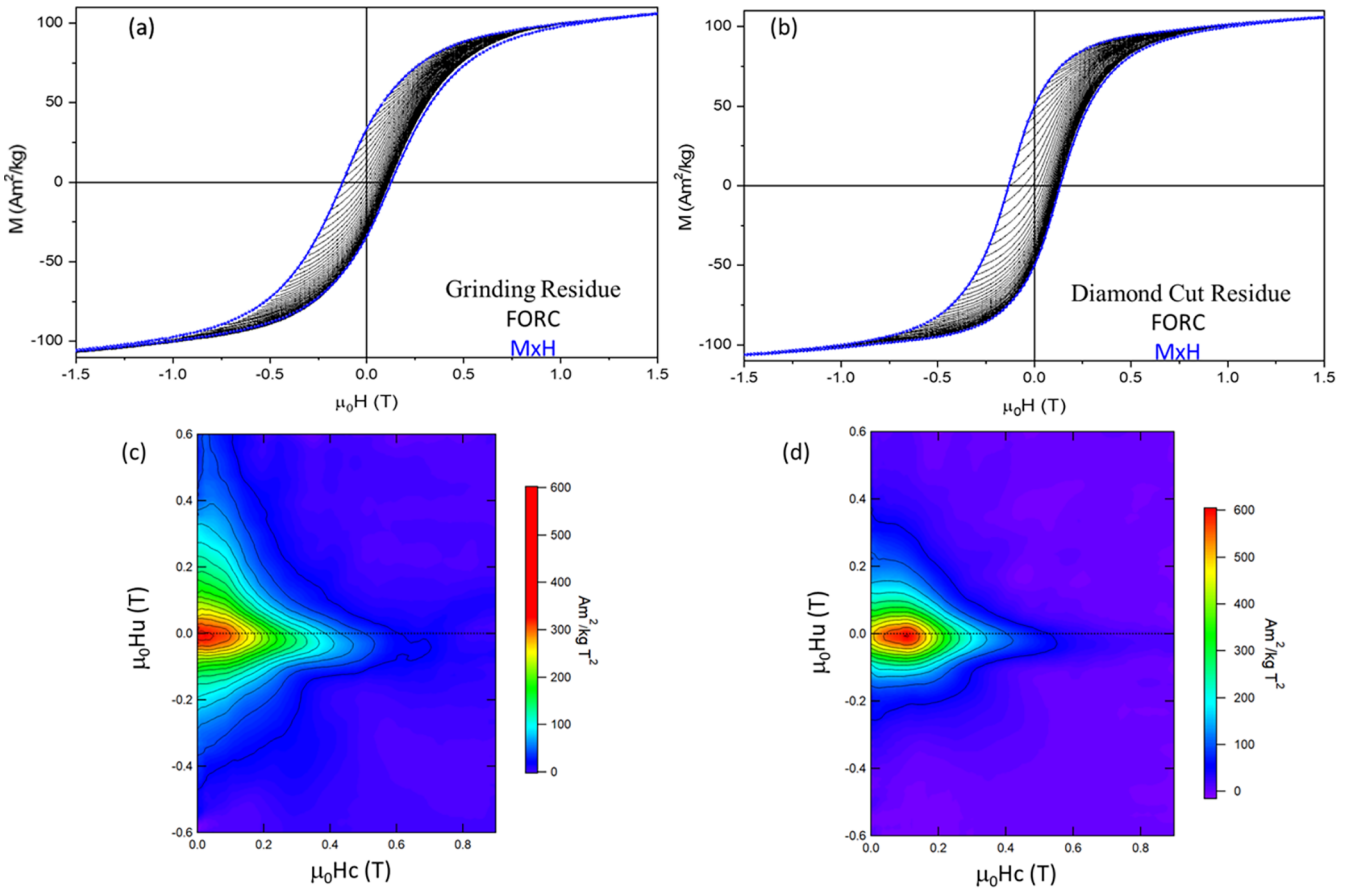

Figure 6. VSM hysteresis curves in blue and FORC measurements in black, respectively: (a) grinding residue and (b) diamond cut residue. 2D FORC distribution of switching fields (H_C) and interaction fields (H_U) for samples: (c) grinding residue and (d) diamond cut residue.

Table 5. Values of Coercivity, Magnetization, and Magnetic Remanence, Obtained from Major Hysteresis Curves[a]

	H_C (±0.0002 T)	*M (±0.1 Am²/kg)	M_R (±0.1 Am²/kg)
(a) Grinding residue	0.1248	86.6	33.7
(b) Diamond cut residue	0.1331	93.6	49.9

[a]*M values were obtained at a maximum applied field of 1.5 T and by subtracting the paramagnetic signal of each sample from the major hysteresis loop.

toward the H_U axis, characteristic of multidomain-like particles. Roberts et al.[58] identified such cases as PSD domain behavior.

A Day diagram[59] expressing the shape of hysteresis loops in terms of coercivity ratio H_{CR}/H_C and the remanence ratio M_{RS}/M_S (also known as squareness) was obtained from the major hysteresis loops in Figure 6. It is used to determine the domain state of magnetization along with summarizing the major magnetic properties of samples. The values of the Day Plots obtained from the major hysteresis loops in Figure 6a,b show an SD state for the diamond cut residue, while the grinding residue shows a PSD state.

The irreversible coercivity distributions (ICDs) obtained from FORC data indicate the point where the irreversibility starts in the FORC curve of diamond cut residue and grinding residue, as shown in Figure 7. The irreversible coercivity values for the diamond cut residue and grinding residue are around 0.1030 and 0.0909 T, respectively.

In summary, the characterization techniques demonstrated that the $Nd_2Fe_{14}B$ phase was degraded in the machining processes. XRD data showed the presence of nondegraded $Nd_2Fe_{14}B$ and $Nd(OH)_3$, while MS analysis indicated a $Nd_2Fe_{14}B$ phase with modification in the iron vicinities as well as a nondegraded $Nd_2Fe_{14}B$, α-Fe, ferrihydrite, and iron phases (Fe^{2+} and Fe^{3+}). XPS data confirmed that the $Nd_2Fe_{14}B$ phase degradation starts at the surface of the particles with the segregation of rare-earth elements. Regarding the particle size analysis, both machining residues presented a nonmodal particle size distribution. All of these characteristics along with the oxygen and carbon contamination found on both residues contributed to changes in the magnetic properties of the residues detectable by VSM and FORC analysis.

CONCLUSIONS

Sintered Nd−Fe−B magnet machining wastes are promising materials for recycling due to their high content of critical rare-earth elements. The process used to machine sintered magnets has significant effects on the properties of the machining sludge, making it especially important to understand the effect of each step of the recycling route on the magnetic properties of the sludge generated. Based on chemical, structural, and magnetic characterization, this work identified that the machining residues present degradation effects due to machining processes that hamper the direct reuse of those residues in the magnet production chain.

It was possible to evaluate the degradation of the grinding and diamond cut machining residues both on the surface and

https://doi.org/10.1021/acsomega.2c08249
ACS Omega 2023, 8, 12246−12258

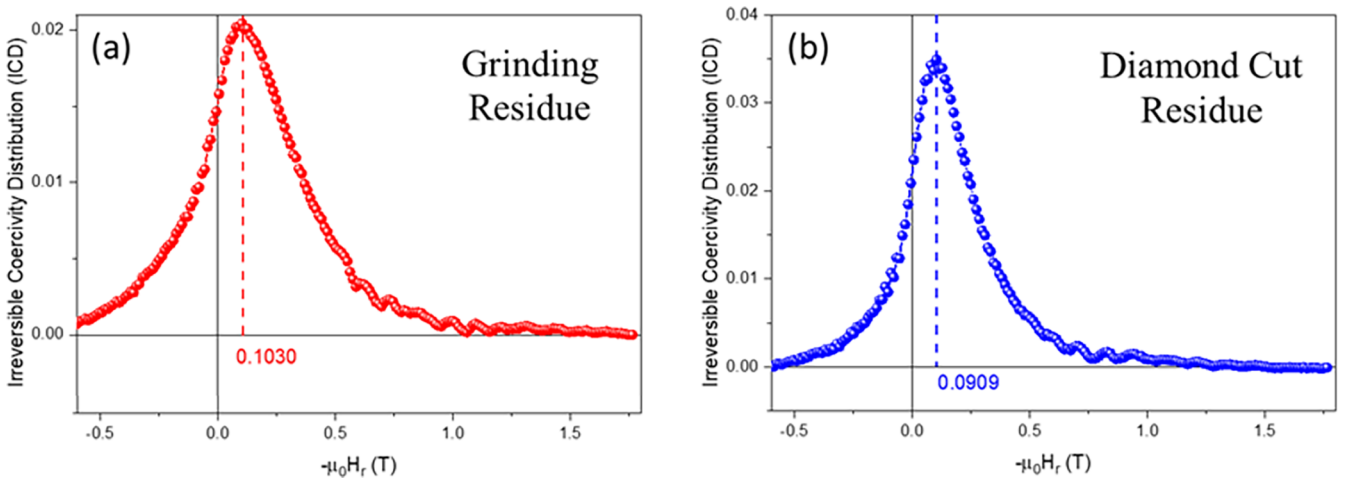

Figure 7. ICD of the (a) grinding residue and (b) diamond cut residue. ($-H_R$) corresponds to the coercivity of remanence.

bulk scale by using characterization techniques with different sensitivities and depths of analysis. These particularities led to different results among the techniques used in this work. Some of the reasons to the differences found are, for example, that ^{57}Fe MS has specific sensitivity for the iron environment. Also, the techniques have different depths of analysis, for example, XPS measurements allowed us to get surface information, while XRD analysis revealed volumetric information. Also, in XRD measurements, the presence of a majoritarian phase can occult others, especially in polycrystalline samples without a defined texture where there are multiple diffraction peaks.

The structural and magnetic properties of machining sludges from cutting and grinding operations demonstrated that there is a partial degradation of the $Nd_2Fe_{14}B$ phase and also changes in the vicinity of the Fe atoms in the $Nd_2Fe_{14}B$ phase. Moreover, regarding the Nd-rich phase, the use of water in the machining fluid results in $Nd(OH)_3$ due to its oxidation. XPS data indicated that the onset of phase degradation occurs at the surface of the residues.

The magnetic properties (remanence and coercivity) of both residues are reduced due to contaminants and the occurrence of other phases, different from the $Nd_2Fe_{14}B$ phase. Magnetic characterization allowed the differentiation among the magnetization states of the grinding and diamond cut residues. The grinding residue shows a pseudo-domain state, while the diamond cut residue shows an SD state.

Before proceeding to reuse these materials for magnet manufacturing, a selection of particle size is required. The widespread particle sizes obtained during machining processes result in the spread of magnetic behavior. FORC measurements showed that the sludge samples studied have complex magnetic behavior due to size-dependent effects on coercivity and the distribution of interactions. The selection of samples with monomodal particle size distribution would assist in the interpretation of their magnetic behavior and the selection of the materials according to future magnet applications.

The comparison of data obtained from the detailed characterization of residues from different machining processes allows us to conclude that the differences found in grinding residues and diamond cut residues are caused by machining process particularities such as heat dissipation mechanisms, machining tools, and fluids.

Nevertheless, raw materials obtained from waste sludges contained significant amounts of the tetragonal phase of Nd–Fe–B which justify the recycling effort to recover directly the ferromagnetic phase required for the production of new and greener magnets. However, to use these materials for permanent magnet manufacture, further processing should be applied to obtain magnetic anisotropy values required for the selected application.

AUTHOR INFORMATION

Corresponding Authors

Karen Bolis − *Nuclear Technology Development Center, CDTN, Belo Horizonte 31270-901 Minas Gerais, Brazil; Laboratory-Factory of Rare Earth Alloys and Magnets (LabFabITR), Lagoa Santa 33400-000 Minas Gerais, Brazil*; orcid.org/0000-0002-9177-5105; Email: karen.bolis@cdtn.br

Luis Eugenio Fernandez-Outon − *Department of Physics—Federal University of Minas Gerais (UFMG), Belo Horizonte 31270-901 Minas Gerais, Brazil*; Email: outon@fisica.ufmg.br

José Domingos Ardisson − *Nuclear Technology Development Center, CDTN, Belo Horizonte 31270-901 Minas Gerais, Brazil*; Email: jdr@cdtn.br

Authors

Gabriela Silva Goulart − *Nuclear Technology Development Center, CDTN, Belo Horizonte 31270-901 Minas Gerais, Brazil*

Alisson Carlos Krohling − *Nuclear Technology Development Center, CDTN, Belo Horizonte 31270-901 Minas Gerais, Brazil*

Renato Mendonça − *Nuclear Technology Development Center, CDTN, Belo Horizonte 31270-901 Minas Gerais, Brazil*

Complete contact information is available at: https://pubs.acs.org/10.1021/acsomega.2c08249

Notes

The authors declare no competing financial interest.

ACKNOWLEDGMENTS

The authors would like to thank CDTN/CNEN for the used characterization infrastructure, LabFabITR and CODEMGE for the grinding machining residues, IPT/USP, LabCri/UFMG, and Microscopy center/UFMG for the realization of

contaminant content analysis, XRD data, and SEM images. The authors would also like to thank CNPq, CAPES, and FAPEMIG for financial support (CNPq - grant-311697/2020-8 and 302867/2022-8).

REFERENCES

(1) Smith, B. J.; Riddle, M. E.; Riddle, M. R.; Earlam, C.; Iloeje, D.; Diamond, D. *Rare earth permanent magnets - Supply chain deep dive assessment*; United States: N. p., 2022.
(2) Constantinides, S. Market Outlook for Ferrite, Rare Earth and other Permanent Magnets *The International Forum on Magnetic Applications, Technologies & Materials*; Jacksonville, 2016.
(3) Klossek, P.; Kullik, J.; van den Boogaart, K. G. A systemic approach to the problems of the rare earth market. *Resour. Pol.* **2016**, *50*, 131−140.
(4) Diehl, O.; Schönfeldt, M.; Brouwer, E.; Dirks, A.; Rachut, K.; Gassmann, J.; Güth, K.; Buckow, A.; Gauß, R.; Stauber, R.; Gutfleisch, O. Towards an Alloy Recycling of Nd−Fe−B Permanent Magnets in a Circular Economy. *J. Sustain. Metall.* **2018**, *4*, 163−175.
(5) Yuksekdag, A.; Kose-Mutlu, B.; Siddiqui, A. F.; Wiesner, M. R.; Koyuncu, I. A holistic approach for the recovery of rare earth elements and scandium from secondary sources under a circular economy framework − A review. *Chemosphere* **2022**, *293*, 133620.
(6) Bonfante, M. C.; Raspini, J. P.; Fernandes, I. B.; Fernandes, S.; Campos, L. M. S.; Alarcon, O. E. Achieving Sustainable Development Goals in rare earth magnets production: A review on state of the art and SWOT analysis. *Renew. Sustain. Energy Rev.* **2021**, *137*, 110616.
(7) Raspini, J. P.; Bonfante, M. C.; Cúnico, F. R.; Alarcon, O. E.; Campos, L. M. S. Drivers and barriers to a circular economy adoption: a sector perspective on rare earth magnets. *J. Mater. Cycles Waste Manag.* **2022**, *24*, 1747−1759.
(8) Ciacci, L.; Vassura, I.; Cao, Z.; Liu, G.; Passarini, F. Recovering the "new twin ": Analysis of secondary neodymium sources and recycling potentials in Europe. *Resour. Conserv. Recycl.* **2019**, *142*, 143−152.
(9) Machida, K.; Masuda, M.; Suzuki, S.; Itoh, M.; Horikawa, T. Effective Recovery of Nd−Fe−B Sintered Magnet Scrap Powders as Isotropic Bonded Magnets. *Chem. Lett.* **2003**, *32*, 628−629.
(10) Machida, K.; Masuda, M.; Itoh, S.; Horikawa, M.; Horikawa, T. Effective Recovery of Nd−Fe−B Sintered Magnet Scrap Powders as Microwave Absorbing Materials. *Chem. Lett.* **2003**, *32*, 658−659.
(11) Yang, Y.; Walton, A.; Sheridan, R.; Güth, K.; Gauß, O.; Gutfleisch, O.; Buchert, M.; Steenari, B.-M.; Van Gerven, T.; Jones, P. T.; Binnemans, K. REE Recovery from End-of-Life NdFeB Permanent Magnet Scrap: A Critical Review. *J. Sustain. Metall.* **2017**, *3*, 122−149.
(12) Fujisaki, J.; Furuya, A.; Uehara, Y.; Shimizu, K.; Ataka, T.; Tanaka, T.; Oshima, H.; Ohkubo, T.; Hirosawa, S.; Hono, K. Micromagnetic simulation of the orientation dependence of grain boundary properties on the coercivity of Nd−Fe−B sintered magnets. *AIP Adv.* **2016**, *6*, 056028.
(13) Kim, A. S. Effect of oxygen on magnetic properties of Nd−Fe−B magnets. *J. Appl. Phys.* **1988**, *64*, 5571−5573.
(14) Costa, I.; Oliveira, M. C. L.; de Melo, H. G.; Faria, R. N. The effect of the magnetic field on the corrosion behavior of Nd−Fe−B permanent magnets. *J. Magn. Magn. Mater.* **2004**, *278*, 348−358.
(15) Namkung, S.; Kim, D. H.; Jang, T. S. Effect of particle size distribution on the microstructure and magnetic properties of sintered NdFeB magnets. *Rev. Adv. Mater. Sci.* **2011**, *28*, 185−189.
(16) Edgley, D. S.; Le Breton, J. M.; Steyaert, S.; Ahmed, F. M.; Harris, I. R.; Teillet, J. Characterization of high temperature oxidation of NdFeB magnets. *J. Magn. Magn. Mater.* **1997**, *173*, 29−42.
(17) Skulj, I.; Evans, H. E.; Harris, I. R. Oxidation of NdFeB-type magnets modified with additions of Co, Dy, Zr and V. *J. Mater. Sci.* **2008**, *43*, 1324−1333.
(18) Farr, M. A study on the impact of surface and bulk oxidation on the recyclability of NdFeB magnets; Diss. University of Birmingham, 2013. http://etheses.bham.ac.uk/id/eprint/4541, December 15, 2022.
(19) Tokuhara, K.; Hirosawa, S. Corrosion resistance of Nd−Fe−B sintered magnets. *J. Appl. Phys.* **1991**, *69*, 5521−5523.
(20) McCain, S. Characterization of the aqueous corrosion process in NdFeB melt-spun ribbon and MQI bonded magnets; Diss. University of Birmingham, 2012. http://etheses.bham.ac.uk/id/eprint/3680, December 12, 2022.
(21) Zhang, X.; Ma, Y.; Zhang, B.; Li, Y.; Lei, M.; Wang, F.; Zhu, M.; Wang, X. Corrosion behavior of hot-pressed nanocrystalline NdFeB magnet in a simulated marine atmosphere. *Corros. Sci.* **2014**, *87*, 156−166.
(22) Li, Y.; Evans, H. E.; Harris, I. R.; Jones, I. P. The Oxidation of NdFeB Magnets. *Oxid. Met.* **2003**, *59*, 167−182.
(23) Kumari, A., Jha, M. K., Pathak, D. D.. Review on the Processes for the Recovery of Rare Earth Metals (REMs) from Secondary Resources. Rare Metal Tech. TMS 2018. *The Minerals, Metals & Materials Series*. Springer, Cham. DOI: 10.1007/978-3-319-72350-1_5
(24) Brião, G. de V.; da Silva, M. G.; Vieira, M. G. A. Adsorption potential for the concentration and recovery of rare earth metals from NdFeB magnet scrap in the hydrometallurgical route: A review in a circular economy approach. *J. Clean. Prod.* **2022**, *380*, 135112.
(25) Jin, H.; Afiuny, P.; McIntyre, T.; Yih, Y.; Sutherland, J. W. Comparative Life Cycle Assessment of NdFeB Magnets: Virgin Production versus Magnet-to-Magnet Recycling. *Procedia CIRP* **2016**, *48*, 45−50.
(26) Yin, X.; Liu, M.; Wan, B.; Zhang, Y.; Liu, W.; Wu, Y.; Zhang, D.; Yue, M. Recycled Nd−Fe−B sintered magnets prepared from sludges by calcium reduction-diffusion process. *J. Rare Earths* **2018**, *36*, 1284−1291.
(27) Haider, S. K.; Lee, J. Y.; Kim, D. Y. S.; Kang, Y. S. Eco-Friendly Facile Three-Step Recycling Method of (Nd-RE)2Fe14B Magnet Sludge and Enhancement of (BH)max by Ball Milling in Ethanol. *ACS Sustainable Chem. Eng.* **2020**, *8*, 8156−8163.
(28) Xu, H.; Wang, F.; Lu, Q.; Qiu, Y.; Liu, W.; Chen, J.; Yi, X.; Yue, M. Nd−Fe−B: From sludge waste to powders via purification and modified Ca-reduction reaction process. *J. Magn. Magn. Mater.* **2022**, *543*, 168606.
(29) Xu, H.; Lu, Q.; Li, Y.; Liu, W.; Yi, X.; Wang, Y.; Yue, M. Reaction mechanism of Ca-reduction diffusion process used for sustainable recycling Nd−Fe−B sludge. *J. Alloys Compd.* **2022b**, *909*, 164744.
(30) Horikawa, T.; Miura, K.; Itoh, M.; Machida, K. Effective recycling for Nd−Fe−B sintered magnet scraps. *J. Alloys Compd.* **2006**, *408−412*, 1386−1390.
(31) Yue, M.; Yin, X.; Li, X.; Li, M.; Li, X.; Liu, W.; Wu, Y.; Zhang, D.; Chen, J.; Yi, X.; Zuo, T. Recycling of Nd−Fe−B Sintered Magnets Sludge via the Reduction-Diffusion Route to Produce Sintered Magnets with Strong Energy Density. *ACS Sustainable Chem. Eng.* **2018**, *6*, 6547−6553.
(32) Asabe, K.; Saguchi, A.; Takahashi, W.; Suzuki, R. O.; Ono, K. Recycling of rare earth magnet scraps: Part I carbon removal by high temperature oxidation. *Mater. Trans.* **2001**, *42*, 2487−2491.
(33) Nakamoto, M.; Kubo, K.; Katayama, Y.; Tanaka, T.; Yamamoto, T. Extraction of Rare Earth Elements as Oxides from a Neodymium Magnetic Sludge. *Metall. Mater. Trans. B* **2012**, *43*, 468−476.
(34) Kruse, S.; Raulf, K.; Trentmann, A.; Pretz, T.; Friedrich, B. Processing of Grinding Slurries Arising from NdFeB Magnet Production. *Chem. Ing. Tech.* **2015**, *87*, 1589−1598.
(35) Kruusing, A.; Leppävuori, S.; Uusimäki, A.; Petrêtis, B.; Makarova, O. Micromachining of magnetic materials. *Sens. Actuators, A* **1999**, *74*, 45−51.
(36) Annapragada, A.; Adjei, A. An analysis of the Faunhofer diffraction method for particle size distribution analysis and its application to aerosolized sprays. *Int. J. Pharm.* **1996**, *127*, 219−227.
(37) ISO13320. *Particle Size Analysis - Laser Diffraction Methods, Part 1: General Principles*, 2009.
(38) Singer, L. Rapid Determination of Oxygen in Steel. *Ind. Eng. Chem., Anal. Ed.* **1940**, *12*, 127−130.

https://doi.org/10.1021/acsomega.2c08249
ACS Omega 2023, 8, 12246−12258

(39) Rodríguez-Carvajal, J. Recent advances in magnetic structure determination by neutron powder diffraction. *Physica B* **1993**, *192*, 55−69.
(40) Brand, R. A. *Normos Mössbauer fit program*; Laboratorium für Angewandte Physik: Duisburg, 1990.
(41) Pike, C. R.; Roberts, A. P.; Verosub, K. L. Characterizing interactions in fine magnetic particle systems using first order reversal curves. *J. Appl. Phys.* **1999**, *85*, 6660.
(42) Roberts, A. P.; Heslop, D.; Zhao, X.; Pike, C. R. Understanding fine magnetic particle systems through use of first-order reversal curve diagrams. *Rev. Geophys.* **2014**, *52*, 557−602.
(43) Blanco-Mantecón, M.; O'Grady, K. Grain size and blocking distributions in fine particle iron oxide nanoparticles. *J. Magn. Magn. Mater.* **1999**, *203*, 50−53.
(44) Long, G. J.; Kulasekere, R.; Pringle, O. A.; Grandjean, F.; Buschow, K. H. J. A comparison of the Mössbauer effect spectra of $R_2Fe_{14}B$ and $R_2Fe_{14}C$. *J. Magn. Magn. Mater.* **1992**, *117*, 239−250.
(45) Kamal, R.; Andersson, Y. Mössbauer spectroscopic studies of $Nd_2Fe_{14}B$. *Phys. Rev. B* **1985**, *32*, 1756−1761.
(46) Givord, D.; Li, H. S.; Tasset, F. Polarized neutron study of the compounds $Y_2Fe_{14}B$ and Nd2Fe14B. *J. Appl. Phys.* **1985**, *57*, 4100−4102.
(47) Wang, J.; Liang, L.; Zhang, L.; Sun, L.; Hirano, S. Deduction of the chemical state and the electronic structure of $Nd_2Fe_{14}B$ compound from X-ray photoelectron spectroscopy core-level and valence-band spectra. *J. Appl. Phys.* **2014**, *116*, 163917.
(48) Kaczmarek, S. M.; Tomaszewicz, E.; Moszyński, D.; Jasik, A.; Leniec, G.; DTA/TG, I. R. EPR and XPS studies of some praseodymium (III) tungstates. *Mater. Chem. Phys.* **2010**, *124*, 646−651.
(49) Mekki, A.; Ziq, Kh. A.; Holland, D.; McConville, C. F. Magnetic properties of praseodymium ions in Na_2O-Pr_2O_3-SiO_2 glasses. *J. Magn. Magn. Mater.* **2003**, *260*, 60−69.
(50) Fortuño-Morte, M.; Beltrán-Mir, H.; Cordoncillo, E. Study of the role of praseodymium and iron in an environment-friendly reddish orange pigment based on Fe doped $Pr_2Zr_2O_7$: A multifunctional material. *J. Alloys Compd.* **2020**, *845*, 155841.
(51) Mullet, M.; Guillemin, Y.; Ruby, C. Oxidation and deprotonation of synthetic Fe^{II}-Fe^{III} (oxy)hydroxycarbonate Green Rust: An X-ray photoelectron study. *J. Solid State Chem.* **2008**, *181*, 81−89.
(52) Albuquerque, A. S.; Tolentino, M. V. C.; Ardisson, J. D.; Moura, F. C. C.; de Mendonça, R.; Macedo, W. A. A. Nanostructured ferrites: Structural analysis and catalytic activity. *Ceram. Int.* **2012**, *38*, 2225−2231.
(53) Liu, M.; Cheng, X.; Li, X.; Pan, Y.; Li, J. Effect of Cr on the passive film formation mechanism of steel rebar in saturated calcium hydroxide solution. *Appl. Surf. Sci.* **2016**, *389*, 1182−1191.
(54) Harrison, R. J.; Feinberg, J. M. FORCinel: An improved algorithm for calculating first-order reversal curve distributions using locally weighted regression smoothing. *Geochem., Geophys., Geosyst.* **2008**, *9*, a.
(55) Schrefl, T.; Shoji, T.; Winklhofer, M.; Oezelt, H.; Yano, M.; Zimanyi, G. First order reversal curve studies of permanent magnets. *J. Appl. Phys.* **2012**, *111*, 07A728.
(56) Hono, K.; Sepehri-Amin, H. Strategy for high-coercivity Nd−Fe−B magnets. *Scr. Mater.* **2012**, *67*, 530−535.
(57) Ramesh, R.; Srikrishna, K. Magnetization reversal in nucleation-controlled magnets. I. Theory. *J. Appl. Phys.* **1988**, *64*, 6406−6415.
(58) Roberts, A. P.; Pike, C. R.; Verosub, K. L. FORC diagrams: A new tool for characterizing the magnetic properties of natural samples. *J. Geophys. Res. Solid Earth* **2000**, *105*, 28461−28475.
(59) Day, R.; Fuller, M.; Schmidt, V. A. Hysteresis properties of titanomagnetites: Grain size and composition dependence. *Phys. Earth Planet. In.* **1977**, *13*, 260−267.

https://doi.org/10.1021/acsomega.2c08249
ACS Omega 2023, 8, 12246−12258